Soft Matter

PAPER

View Article Online
View Journal | View Issue

Cite this: *Soft Matter*, 2025, **21**, 7433

High throughput estimates of surface tension using steady droplet deformation in pressure-driven fluidic flows

Evyatar Shaulsky, †[a] Sabrina Marnoto, †[a] Avi J. Patel[a] and Sara M. Hashmi *[abc]

Advances in fluidic droplet generation both necessitate and enable accessible, high throughput methods to optimize formulations by measuring surface tension. One fluidic approach involves creating extensional flow using constrictions. Droplets deform within a constriction, and then experience extensional flow upon exiting into a wider channel. Transient relaxation of the deformed droplets, coupled with the details of the extensional flow, can be used to measure surface tension. We propose an alternative, arguably simpler approach: we use steady deformation within a constriction to measure surface tension. Our approach is motivated by the linear theories that describe droplet deformation in steady flows. These theories, encompassing both clean and surfactant covered drops in unbounded and bounded shear flows, show that droplet deformation is linear with the capillary number for small deformations. Interestingly, this steady deformation approach to estimating the capillary number, and thus, surface tension, has not been tested in pressure driven microfluidic flows. We generate and flow emulsion droplets through a series of increasingly narrow constrictions and use steady deformation to measure surface tension. We investigate both water-in-oil and oil-in-water droplets, stabilized by three different surfactants over a range of concentrations. In a subset of experiments, we vary the viscosity ratio by adding polyethylene glycol diacrylate to water droplets. Validation using both the transient deformation fluidic approach and pendant drop measurements on individual droplets demonstrates the viability of using linear scaling behavior to estimate surface tension. Our results suggest steady state deformation in pressure driven flows can be used to measure surface tension even when droplets are slightly confined. This steady droplet deformation approach to surface tension measurements represents a readily-accessible option for those using fluidic droplet generators to perform biomedical or other assays, or to investigate or optimize emulsion formulations.

Received 13th May 2025,
Accepted 27th August 2025

DOI: 10.1039/d5sm00493d

rsc.li/soft-matter-journal

I. Introduction

Droplets play a critical role in many consumer product industries such as cosmetics, food, and pharmaceuticals. Droplets form by mixing two immiscible liquids to create emulsions. Bulk emulsification methods yield large droplet quantities, but droplets are typically polydisperse, which can cause emulsion instability and other undesired effects.[1,2] Microfluidic techniques can generate highly reproducible monodisperse droplets, with massive parallelization able to counteract the low yield of microscopic techniques.[3–5] In fluidics, the transition between "jetting" and "dripping" regimes of flow and the success of droplet pinch-off is governed by a complex interplay of viscous stresses and capillary effects.[6] In experimental practice, the stability and reproducibility of droplet formation is controlled by the viscosity ratio of the inner and outer phases and the flow rates or pressure drops driving each fluid phase. Typically a more viscous outer, continuous phase more readily facilitates pinch-off of less viscous droplets.[6] Creative use of multiple inlets and droplet pinch-off geometries combined with precise flow rate control enables generation of double-, triple-, and a variety of designer emulsions.[7–9] Fluidics can even be used to generate and control coalescence in Pickering emulsions,[10–12] with the possibility of optimizing surface coverage using AI methods.[13] Droplet microfluidics extend to biological fields with singe-cell encapsulation; cells are encapsulated within aqueous droplets surrounded by a controlled micro-environment and independently analyzed downstream.[14–16]

[a] *Department of Chemical Engineering, Northeastern University, Boston, MA 02115, USA. E-mail: s.hashmi@northeastern.edu*
[b] *Department of Mechanical and Industrial Engineering, Northeastern University, Boston, MA 02115, USA*
[c] *Department of Chemistry and Chemical Biology, Northeastern University, Boston, MA 02115, USA*
† These authors contributed equally to this work.

The extensive use of microfluidics for droplet generation highlights the growing need to measure and control liquid–liquid interfacial properties in-line. Surface tension controls droplet properties such as shape, size, stability, and coalescence.[17–20] Reducing surface tension typically requires adding surfactants or polymers, but excess adsorbent can lead to micelle formation and foaming instability.[21,22] Additionally, Marangoni stresses arise from gradients in surface tension, further leading to droplet instability. Common techniques to measure droplet surface tension include pendant droplet, sessile droplet, and spinning droplet techniques.[23–25] However, these require measurements of one droplet at a time, limiting their utility for optimizing fluidics-based emulsion formulation chemistry. Further, these techniques each require separate benchtop instrumentation.

Microfluidic techniques can mimic some of these macro-scale measurements of surface tension. Several of these fluidic techniques require immobilization of a drop, and one drop must be measured at a time. Droplet shape can be oscillated by the application of an electric field to measure surface tension.[24,26] Hydrodynamic forces such as inertial and viscous forces also induce droplet oscillations, even for nearly spherical droplets at constant surface tension.[27] Droplets can be immobilized in a region of extensional flow and their deformation measured with respect to extension rate.[24,28] Droplets can also be deposited on a cantilever, with the static deflection of the beam used to extract surface tension of the drop.[24,29] However, for these methods, measuring droplet properties requires stationary droplets. As such, this impedes further analysis downstream and negates one of the primary benefits of microfluidics, which is to enable continuous, high throughput micro-scale measurements in flow.

Only one current microfluidic method takes advantage of the high throughput nature of fluidics. In this, droplets deform while flowing through a constriction. Upon exiting, they relax, and the transient behavior is used to measure surface tension.[24] This method leverages descriptions of drop deformation in external flow fields dating back to the original work of G. I. Taylor.[30] Subsequent theoretical treatment describes the transient behavior of deforming drops.[31] Recent implementations that measure deformation dynamics extract surface tension from the shape of the deformed droplets in extensional flows through cylindrical capillaries or microfluidic devices made in PDMS.[32–36] In these implementations, the fluidic designs include geometric features that involve either sudden expansions or constrictions in the width of the channel. When flow rate is constant, conservation of mass requires that droplets decelerate upon entering an expansion or accelerate upon entering a constriction. Any deformation of a droplet within a constriction relaxes back to a sphere upon exit. Measuring both the time-dependent droplet shape and the variation in the extension rate enables surface tension measurements. Because both droplet velocity and shape change in time and space at the exit of a constriction, we refer to this type of surface tension measurement in flow as the ''transient'' method.

While transient deformation relaxation provides a robust measurement of surface tension, we propose an even simpler implementation of small droplet deformation theories in pressure driven flows. Rather than measure surface tension of droplets as the shape changes in extensional flow, we measure the steady deformation of a droplet in steady flow within a constriction. We demonstrate these measurements using a relatively simple geometric channel design. Our design allows for in-line measurements of deformation over a range of applied viscous stresses without requiring manual adjustment to input flow rates or driving pressure. We first generate droplets in a flow-focusing pinch-off device. They then flow through a channel with constrictions of increasingly narrow width. Because droplets are driven at a constant flow rate, they experience increasingly higher velocities as they navigate the constrictions, and therefore increasingly higher shear stresses. Video analysis provides simultaneous measurements of steady droplet velocity and steady deformation, from which we calculate surface tension. In both the transient and steady approaches, surface tension measurements are taken after surfactant equilibrates on the droplet interface.[36]

We measure the surface tension of several different emulsion systems, both water-in-oil and oil-in-water droplets, using three different surfactants, both ionic and non-ionic. We validate our steady deformation measurements by two independent methods: the pendant droplet technique and the fluidic transient deformation relaxation method summarized above. In a subset of measurements, we modify the viscosity ratio by adding a polymer to the water droplets. For this we choose PEGDA, a long chain polymer that forms a blank stale hydrogel when mixed with a photoinitiator and exposed to UV light, commonly used in fluidic microgel production.[4,37] Control of droplet surface tension and stability of PEGDA-filled water droplets before crosslinking are required to optimize particle making. We find that all measurements using the steady state method compare well with the transient method and pendant drop. Remarkably, we find that steady state droplet deformation can provide accurate measures of surface tension, regardless of the emulsion system, even when droplets are somewhat confined in the vertical dimension due to the height of the channels. We anticipate that the simplicity of steady deformation measurements may enable greater access to fluidic tensiometry for a wide variety of in-line measurement needs.

II. Materials and methods

A. Sample materials

We measure the surface tension of both water droplets in oil and oil droplets in water in our flow tests. To measure surface tension σ we use three different surfactants in our experiments: Span 80 (Sigma-Aldrich, CAS 1338-43-8), Tween 80 (Sigma-Aldrich, CAS 9005-65-6) and sodium dodecyl sulfate (SDS) (Sigma-Aldrich, CAS 151-21-3). The oil phase is a light mineral oil (Fisher, CAS 8042-47-5). In all cases, surfactant is introduced through the continuous phase. Span 80 and Tween 80 are used

to create water drops in oil at mole fractions ranging from $\chi = 10^{-5}$ to 10^{-1}. For flow tests where we measure oil droplets in water, we add either Tween 80 or SDS to the continuous phase, with concentration ranges from $\chi = 0.00125$ to $\chi = 0.01$.

For the system of water droplets in oil, we adjust the inner phase viscosity by dissolving polyethylene glycol diacrylate (PEGDA) with molecular weight 700 (Sigma-Aldrich, CAS 26570-48-9) in DI water at concentrations c = 9, 19, 29 and 39% by volume. We add 1% by volume photoinitiator 2-hydroxy-2-methylpropiophenone (Sigma-Aldrich, CAS 7473-98-5) to the aqueous droplet phase. In this way, the PEGDA droplets we investigate mimic the droplet chemistry used as precursors to hydrogel particle formation. Note that we do not expose the PEGDA droplets to UV in this study.

We measure viscosity μ of the inner and outer fluids using a standard shear rate sweep protocol at room temperature, in a cone-and-plate geometry in a rheometer (TA DHR; 2^0, 60 mm cone). The mineral oil has $\mu = 39.5 \pm 1.6$ mPa s. The aqueous phase viscosity depends on PEGDA concentration: μ = 0.89, 1.47, 2.46, 4.23 and 7.77 mPa s for c = 0, 9, 19, 29 and 39%, respectively. For water drops in mineral oil, the viscosity ratio between the inner and outer liquid phases is $\lambda = 0.02$, increasing to $\lambda = 0.20$ when PEGDA is present in the water drops at c = 39%. For oil drops in water, $\lambda = 44$.

B. Device design

The microfluidic design consists of two main stages: droplet formation and deformation measurement. The first stage, shown in Fig. 1a, is a flow-focusing droplet maker that enables the production of uniform droplets that flow in single file. At the neck junction, the inner droplet fluid in inlet (1) is pinched off by the outer continuous fluid from inlet (2). Droplets then flow into a gradually expanding channel. At the downstream position where the channel width has increased by a factor of two, additional continuous phase from inlet (3) is used to control the linear velocity.[33,34] Flow through inlet (3) controls the distance between droplets and facilitates particle tracking.

We employ three different device geometries to measure droplet deformation. Two of these measure deformation in steady flow while the third measures deformation as a function of time in transient flow. In one variation of the steady flow geometry, Fig. 1b, sequentially narrowing constrictions in channel width are arranged such that all droplets flow in the $+x$ direction. As indicated in Fig. 1a, y indicates the direction across the channel width. Fig. 1b shows a device with four distinct channel widths arranged linearly along the flow path with constrictions narrowing from 195 to 75 μm wide over a total length 2100 μm. We refer to this geometry as the "linear" arrangement of constrictions.

In the second geometry to measure deformation in steady flow, Fig. 1c, constrictions are arranged in switchbacks. The particles flow in the $-x$ direction in the first constriction, then in the $+x$ direction, and so on, as indicated by green arrows. Fig. 1c shows an image of this stacked constriction geometry in which there are five constrictions, with widths narrowing from 195 to 40 μm. The constrictions appear stacked on top of each other when viewed in the microscope. In this "stacked" geometry, the length of each constriction is 3.5 mm, much greater

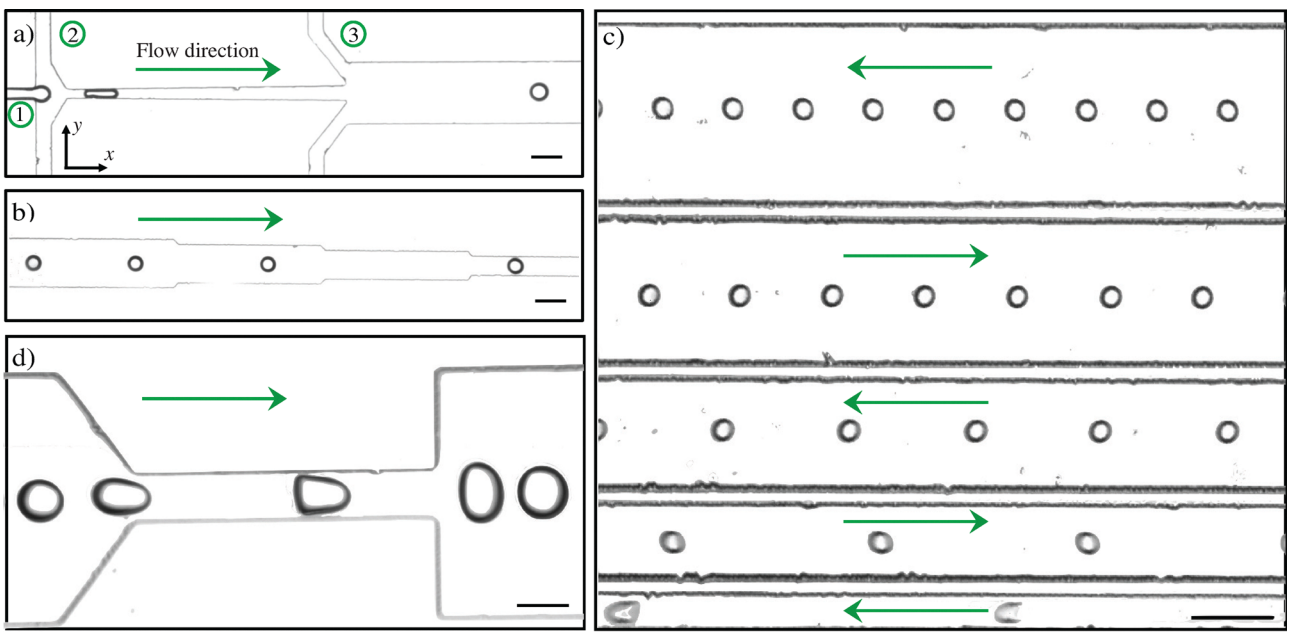

Fig. 1 Microscopy images of the microfluidic flow-focusing droplet maker and variations of the tensiometer geometry. (a) Shows the droplet maker, where an aqueous stream (1) is pinched off by a continuous oil stream (2), and a second junction downstream brings in additional continuous phase (3) to control the velocity of and distance between the droplets. (b) Shows the linear arrangement of microfluidic constrictions downstream of the droplet maker, with channel widths decreasing discretely in the direction of fluid flow. (c) Shows a steady flow geometry where constrictions of increasingly narrow width are stacked on top of each other in a series of switchbacks. (d) Shows a constriction from the transient flow geometry, in which the channel tapers, then abruptly expands to its original width. The scale bars are 100 μm. Green arrows indicate direction of flow.

than the width of the microscope image, which is ~800 μm wide. As such, transitions between switchbacks are well beyond the field of view to the left and to the right. Droplets in the field of view are far from the entrance region of the constrictions. Any shape perturbations due to turns in the channel are likewise beyond the field of view.

The third device geometry, Fig. 1d, measures the relaxation of deformed droplets back to spheres. Droplets flow continuously in $+x$, encountering a series of six individual constrictions followed by expansions. Flow in the main channel of width of ~500 μm converges into constrictions that are between 5 and 10 times narrower than the main channel. At the exit of each constriction, the channel width abruptly returns to its original width of ~500 μm. As such, droplets exiting each constriction decelerate, experiencing an extensional flow rate $\dot{\varepsilon} = dv/dx$ where v is the droplet velocity in the x direction. Droplets that experience deformation within the constriction relax back to spheres upon exiting. In this geometry, transient relaxation is used to measure surface tension, σ.[35,36] We refer to use of this geometry as the "transient" method. Fig. 1d shows an example channel of width 480 μm constricting to 90 μm then expanding back to 480 μm.

All devices are made with polydimethyl siloxane (PDMS) using standard soft lithography methods.[38] In the linear steady flow device, channel height is h = 32.4 μm.[38] In the stacked steady flow device, h = 50 or h = 70 μm. In the transient device, h = 85–105 μm. Both the PDMS and glass slide are treated by plasma (Harrick) and adhered together, with holes punched through the PDMS so that all tubing enters into and exits from the top of the device.

C. Flow tests

Flow through the device is controlled using constant driving pressure (Fluigent LineUp Flow EZ). In all three device geometries, the pressures driving flow through inlet (1) are typically up to 300 mbar. The pressure driving inlets (2) and (3) are typically higher, up to 1000–2000 mbar when the continuous phase is oil, and up to 3000 mbar when the continuous phase is water. At these pressures, the linear velocity of the droplets can reach $v \sim 1$ cm s^{-1}, or even faster for oil droplets in water. The flow rate ratio between the aqueous and oil streams in the neck junction enables control over droplet diameter and production frequency. We control the pressure driving inlets (1) and (2) to maintain droplet diameters $a < h$. In a few cases, we form droplets that are similar in size or slightly larger than h.

The plasma cleaning process described above adheres the glass slide to the PDMS through a hydrophilic interaction, causing the device to remain hydrophilic for at least 3 hours, providing ideal conditions when water is the continuous phase. When oil is the continuous phase, due to the hydrophilic interaction between the drops and the glass slide, we preflush the channel with Aquapel to provide a hydrophobic coating on the PDMS and glass surfaces.[39] This method facilitates droplet flow and prevents adhesion even at low surfactant concentrations. Still, we observe water droplets sticking to the channel walls and blocking the channel in very low surfactant concentration conditions (Fig. S1). This sets a lower limit of $\chi = 3.7 \times 10^{-4}$ for the surfactant concentration measurable in the fluidic device. As surfactant concentration increases, the surface tension decreases, leading to better control of both droplet production frequency and droplet size.

D. Microscopy

All fluidic devices are imaged on a Leica inverted microscope (DMi8) using either a 5×, 10×, or 20× objective. The linear arrangement facilitates imaging all four constrictions simultaneously using the 5× objective, with resolution 0.96 pixels per μm. We can also view one constriction at a time with the 20× objective, with resolution 3.33 pixels per μm, capturing four separate videos to image the total device. An example of a 20× image of the linear device is shown in Fig. S2. For the stacked arrangement, we image all constrictions simultaneously regardless of the objective used. For the device measuring transient relaxation, we image droplets at the exit of each constriction independently, using either a 5× or 10× objective. In the devices with stacked constrictions and in those used to measure transient relaxation, droplet residence time is on the order of 10 s between formation and measurement.

Regardless of device geometry, we reduce the field of view in the dimension perpendicular to flow to minimize exposure time. We collect images up to 167 frames per second using an sCMOS camera (Leica DFC9000), or up to 3000 frames per second using a high-speed camera (Photron FASTCAM Mini AX200). There is a tradeoff between resolution in space and resolution in time. Frame rates can be increased when the field of view is cropped. The use of lower magnification objectives allows for cropping of the field of view, thereby enabling a higher frame rate. However, using a higher magnification objective requires a larger region of the field of view to image the flow. Therefore the higher spatial resolution may mean slower frame rates. Between 2–60 s are captured for each flow condition, depending on the frame rate. We collect several thousand frames for each flow test.

Due to the high velocity of the drops, the frame rate of video capture must be sufficiently fast. Most cameras used for microscopy operate using a raster scan. The rolling shutter typically opens from the middle of the image, and the scan speed v_s is half the number of pixels in the vertical dimension of the image divided by the exposure time. Due to convection, the top of the droplet moves forward during the time it takes the shutter to reach its location. If v_s is not sufficiently fast compared to v, still images may show droplets tilted with respect to the flow direction: $\theta = \arctan(v_s/v)$. This artifact can be seen in the second narrowest constriction in Fig. 1c: the major axis of the droplets appears tilted above horizontal. The velocity of the droplets is ~11 000 μm s^{-1} in this constriction, corresponding to $v \sim 160$ pixels per frame. The image resolution and scan speed explains this tilt: $\theta = \arctan(v_s/v) \sim 70^\circ$.

E. Image analysis

Each series of images is analyzed to obtain both droplet position and shape in every frame (Python OpenCV), with the

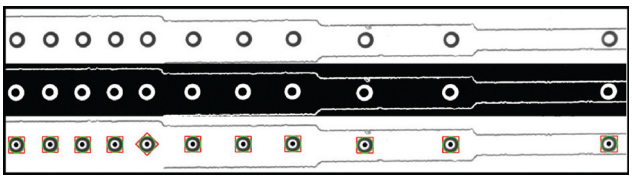

Fig. 2 Image analysis: the first step (top) is the image crop and rotation. In the second step (middle), the images are thresholded and binarized. The last step (bottom) defines the contours in green, the bounding rectangles, in red, and the centroids of each individual droplet in every frame.

steps in the process indicated in Fig. 2. After rotating and cropping the frames so that flow is in the x-direction only, we binarize the grayscale images, as shown in the middle of Fig. 2. We identify all contours in the binary image, and filter by size and maximum deformation to remove artifacts and drops cut off from the ends of the image. The outermost contour of the droplet is indicated in green in the bottom image of Fig. 2.

We test two alternative methods for identifying the location of the droplet centroid and measuring the droplet shape. In one method, after defining the relevant contours, we use the rectangular bounding box around each individual contour, as shown in red in the bottom of Fig. 2. The dimensions of the bounding box give the major and minor axes of the droplet, d_x and d_y, respectively, providing a measure of the droplet shape. The center of the bounding box is the droplet centroid. This method of measuring droplet shape using major and minor axes has been employed in a few instances of extensional flow measurements of droplet deformation.[34,35]

In the second method, we identify all N pixels within a given droplet contour. We calculate the moment of inertia I along each axis by summing the positions of all pixels j within each droplet contour:

$$I_x = \sum_j^N \left(x_j - \langle x\rangle\right)^2 \quad \text{and} \quad I_y = \sum_j^N \left(y_j - \langle y\rangle\right)^2 \tag{1}$$

where $(\langle x\rangle, \langle y\rangle)$ represents the centroid of each contour. The centroid is the mean position of all pixels in x and y; for example, $\langle x\rangle = \frac{1}{N}\sum_j^N x_j$.[40]

In either method of identifying droplet shape, the centroids are then analyzed using a standard particle tracking algorithm to obtain the trajectory and velocity of each droplet.[41]

F. Pendant droplet measurements

We validate the fluidics measurements using the pendant droplet technique.[42] We measure the interfacial tension between water and oil as a function of Span 80 (Sigma CAS 1338-43-8) in the range of mole fractions $\chi = 10^{-5}$ to 10^{-1}. We use one of two instruments: a Krüss DSA-100 instrument, and the platform provided by DropLab Inc. Twelve different surfactant concentrations are prepared in oil and each loaded into a standard cuvette. Then, a DI water droplet with volume on the order of 1 μL is suspended into bulk mineral oil from a 26- or 33-gauge needle. A minimum of five droplet backlit shadow images are acquired for each surfactant concentration. We perform this sequence at least twice: as a result, between 7 and 25 droplets are measured at each surfactant concentration.

The interfacial tension σ is calculated either using an open source analysis tool, OpenDrop, or droplet shape analysis performed by the instrumentation software and based on the Jennings and Pallas algorithm.[43,44] In short, the droplet shape at equilibrium is determined by a balance between gravitational and surface tension stresses. Due to the pendant shape of the droplet, however, the Young–Laplace equation cannot be solved analytically. Instead, the droplet profile is measured as a function of the arc length from the droplet apex using image analysis. The Young–Laplace equation is then used to fit the droplet shape in an iterative manner to obtain σ.[42,45] Similarly to the situation with the microfluidic measurement, at very low surfactant concentration, $\chi < 2 \times 10^{-5}$, the droplet sticks to the needle and the walls of the cuvette in the pendant droplet apparatus, preventing accurate measurements of very high surface tension.

III. Results and discussion

A. Theory: deformation in steady shear flow

Small deformation of droplets has been described in unbounded linear flows for a variety of surfactant coverages, including bare droplets uncovered by surfactant,[30] droplets with mobile interfaces partially covered by surfactant,[46] and for droplets with immobile interfaces due to full coverage by surfactant.[47] In all of these situations, droplet deformation D scales linearly with the capillary number Ca:

$$D = f\mathrm{Ca} \tag{2}$$

where f can be referred to as a proportionality constant, prefactor, or slope of the linear dependence. In $\mathrm{Ca} = \mu\dot{\gamma}r_0/\sigma$, μ is the continuous phase viscosity, r_0 the unperturbed droplet radius, and $\dot{\gamma}$ is the shear rate. In all cases f is a constant of order 1. For bare droplets in unbounded shear or extensional flows, $f(\lambda) = (19\lambda + 16)/(16\lambda + 16)$ depends on the viscosity ratio between the inner droplet and outer continuous phases.[30] This result matches experimental data obtained in both shear and extensional flows, up to $D \sim 0.2$ and $D \sim 0.3$, respectively.[30] For droplets partially covered by surfactant, the amount of surfactant coverage on the mobile droplet interface also determines the prefactor f for small deformations in shear flow. That is, f depends on both λ and a parameter that describes the sensitivity of surface tension to the surfactant concentration on the interface.[46] If the amount of surfactant enables complete coverage of a drop, the interface becomes immobilized. These drops behave like rigid particles. In this case, small drop deformation varies linearly with Ca, and $f = 5/4$ without dependence on the viscosity ratio.[47] At finite deformations, beyond $\mathrm{Ca} \approx 0.2$, analytical models no longer suffice and a boundary integral approach must be used to calculate deformation in shear flow.[46,47]

In bounded flows, with the degree of confinement defined as a/h, deformation remains linearly proportional to Ca both for clean drops and those with immobile interfaces. For clean

drops in unconfined flows, with $\lambda = 1$, $f = 1.09$.[30] As confinement increases f increases, and $D >$ Ca. In bounded shear flows, this effect is intensified for larger Ca.[48] Measurements of the deformation of clean drops obtained at Ca = 0.1, 0.2, and 0.3 match an analytical approach based on the method of reflections up to nearly $a/h \sim 1$.[48,49] For drops with immobile interfaces in confined shear flows, $f = 1 + \frac{8}{5}(a/h)^3$, as long as Ca < 0.2.[50] In this case, f remains $O(1)$ as long as $a/h < 1.7$. In pressure driven Poiseuille flow in a tube, drop deformation is nearly identical to that in shear flow, for $D \lesssim 0.1$.[51]

In all of these small deformation theories, the phenomenology of eqn (2) holds true, with a prefactor constant of order 1. To illustrate this point, we note that Taylor's theory for clean drops suggests values between $f = 1.005$ and 1.03 for the water drops in oil used in our experiments, and $f = 1.18$ for the oil drops in water.[30] At full surfactant coverage of the droplet interface, we expect $f = 1.25$.[47] These values represent a small correction to $D =$ Ca. Therefore, we leverage the universality of this dimensional scaling for small deformation in our measurements, which span a range of surfactant coverages and degrees of confinement. To estimate surface tension from steady droplet deformation, we invert eqn (2) and use

$$\sigma = f\frac{\mu\dot{\gamma}r_0}{D} \tag{3}$$

with $f = 1$.

In our steady flow tests, we employ pressure-driven flow rather than simple shear. We approximate the instantaneous shear rate by the wall shear rate, $\dot{\gamma}$, using the instantaneous droplet velocity and the characteristic length scale of the narrowest channel dimension, namely the half-height of the channel: $\dot{\gamma} = 2v/h$. In our experiments, $\dot{\gamma}$ ranges from $O(1)$ to $O(10\,000)$ s^{-1}, with the highest shear rates used to measure deformation of oil droplets in water.

The deformation parameter D is a measure of the elongation of the droplet, and has been measured using two variations. In the simplest definition,

$$D = \frac{d_x - d_y}{d_x + d_y} \tag{4}$$

where d_x and d_y are the major and minor axis of the droplet, described above.[34,35] Alternatively, droplet deformation can be measured by replacing d_x and d_y with $\sqrt{I_x}$ and $\sqrt{I_y}$.[40] The moments of inertia I are given in eqn (1).

One benefit of using multiple constrictions within a single channel geometry lies in the ability to measure the steady deformation D at multiple shear rates without adjusting the overall pressure drop driving the flow test. The hydraulic resistance remains constant throughout all flow tests, indicating no perturbation of the device geometry, even at high driving pressures. Therefore the pressure-driven flow provides a constant volume flow rate, Q. By conservation of mass, all droplets navigating the narrowing constrictions increase in their linear velocity from one constriction to the next. Droplet flow velocity v increases proportionally with the reduction of the channel cross-sectional area A: $v = Q/A$. In the linear and stacked geometries, droplets experience four or five distinct values of velocity and shear rate, respectively. As such, each individual constriction provides a measurement of σ using eqn (3).

Furthermore, since each population of droplets experiences an increasing velocity along its flow path, we plot D as a function of $\mu\dot{\gamma}r_0$ and calculate σ as the reciprocal of the slope. We measure the goodness of the linear fit of D *versus* $\mu\dot{\gamma}r_0$ as an assessment of the linear behavior of $D \sim$ Ca. We limit our measurements to drops with both steady deformation and steady position within the flow. While droplets migrate across streamlines due to their deformability, our measurements are located well beyond the entrance to the channel, and droplets flow along the center line.[52,53] We refer to these measurements of surface tension as "steady", in reference to the steady flow of the droplets.

B. Theory: deformation in transient flow

As an alternative to measuring droplet deformation in steady flows, surface tension can also be measured in transient extensional flow. The microfluidic equivalent of the four-roller mill originally used by Taylor creates a quasi-static extensional flow, with two outlets arranged perpendicular to two inlets.[54] A droplet is then trapped in the center of the intersection of the four channels, and its shape measured as a function of the rate of extension.

To perform measurements on droplets in extensional flows without trapping them, abrupt changes in the channel cross section are required along the flow path. These changes involve abruptly changing the width of a channel, typically by a factor of 3.[34–36,55] As droplets flow at constant flow rate into or out of a region with an abrupt change in channel width they experience rapid acceleration or deceleration, respectively. The change in velocity along the flow path is the extension rate: $\dot{\varepsilon} = \frac{dv}{dx}$. Upon deceleration at the exit of a constriction, a deformed droplet relaxes back to its undeformed spherical shape.[31,34,35] The dynamics of the relaxation rate of D depend on the extension rate:

$$\frac{\partial D}{\partial t} = \frac{5}{2\lambda + 3}\dot{\varepsilon} - \frac{\sigma}{\alpha\mu r_0}D \tag{5}$$

where α is given by

$$\alpha = \frac{(2\lambda + 3)(19\lambda + 16)}{40(\lambda + 1)} \tag{6}$$

Eqn (5) can be solved analytically, with the result $D(t) = D_0 \exp(-t/\tau)$, where D_0 is the deformation at time 0, or upon exiting a constriction.[31,34,35] The characteristic time $\tau = \alpha\mu r_0/\sigma$. Thus, $\alpha\mu$ represents an effective viscosity of the continuous phase.[34] For droplets of DI water, $\alpha = 1.23$. With PEGDA added at 39% by volume, α increases to 1.40. In our measurements, τ ranges from $O(10^{-4})$ to $O(10^{-3})$ s^{-1}, and the maximum deceleration is $\dot{\varepsilon} \sim O(10)$ s^{-1}.

To measure σ, we apply the chain rule $\frac{\partial D}{\partial t} = \frac{\partial D}{\partial x}\frac{\partial x}{\partial t} = v\frac{\partial D}{\partial x}$ to rearrange eqn (5) into:

$$\alpha\mu\left(\frac{5}{2\lambda+3}\dot{\varepsilon} - v\frac{\partial D}{\partial x}\right) = \sigma\left(\frac{D}{r_0}\right) \quad (7)$$

as is typically done.[31,34,35] An example of $\dot{\varepsilon}$, dx/dt, D, and dD/dt plotted as a function of x is shown in Fig. S3. With D and v measured in every image, the left hand side of eqn (7) is a linear function of D/r_0 with slope σ, as shown in Fig. S4.[34] We refer to these measurements of surface tension as "transient," in reference to the transient dynamics of the droplet shape recovery in extensional flow.

In fluidic geometries which trap a droplet in the center of a quasi-static extensional flow field, $v = 0$, reducing eqn (7) to two terms, and the steady deformation D varies linearly with the extension rate of the flow field.[54]

In experimental practice, surfactants are added to stabilize drops. However, both theoretical approaches described above assume steady surface tension, which requires steady surfactant coverage. In the presence of surfactants, σ reaches equilibrium under two mechanisms: transport of surfactants to the interface and adsorption at the interface.[56] In stationary drops, transport occurs by diffusion, and can be accelerated by increasing the concentration of the surfactant or reducing the size of the droplet. In micron-sized droplets, σ approaches equilibrium orders of magnitude faster than in milli-sized droplets.[36,57–59] When measuring σ in flow, the phase in which surfactant is introduced also affects equilibration of surface coverage. Due to convection, surfactants introduced from the outer phase cause σ to reach equilibrium faster than surfactants introduced in the inner phase.[36] Reaching equilibrium surface coverage is complicated by the fact that flow sweeps surfactants to the back of the droplet, inducing Marangoni stresses.[60] Nonetheless, equilibration of surface tension measurements of flowing droplets occurs within $\sim O(1)$ second for droplets that are tens of microns in diameter with surfactants in the outer phase.[36,56] In our flow tests, surfactant is introduced in the outer, continuous phase. To ensure equilibration, droplets experience a residence time $\sim O(10)$ seconds before reaching the stacked constrictions in which steady deformation is measured.

C. Experimental results

We begin by investigating water droplets in oil, stabilized by Span 80. Fig. 1a and c show example images of droplets flowing through constrictions in the linear and stacked arrangements. Clearly seen in Fig. 1c is the change in droplet shape as they move from the largest constriction (top) to the smallest constriction (bottom). In this image, the water droplets contain 39% PEGDA by volume, the mineral oil contains Span 80 at $\chi = 1 \times 10^{-2}$ mole fraction, and the droplet diameters are $\sim$30 μm. As seen in the narrowest constriction in Fig. 1c, the droplet forms a slipper shape like that seen as Ca $\rightarrow$ 1 in Poiseuille flow.[61] Because the deformed drops are no longer simply elongated, but now have a dimple, we omit the narrowest, fifth constriction from the surface tension analysis that follows.

We measure the instantaneous deformation D and velocity v of all droplets in a flow test as they pass through a series of increasingly narrow constrictions. Fig. 3 shows two representative measurements of v (blue) and D (green) as a function of flow direction x. The data shown in Fig. 3a is obtained from the linear arrangement of constrictions imaged at 5× and the data shown in Fig. 3b comes from a stacked arrangement imaged at 10×. The results in Fig. 3a and b correspond water droplets with $\chi = 1.39 \times 10^{-2}$ and $\chi = 1 \times 10^{-3}$, of Span 80, representing runs 12 and 3 in Table S1, respectively. For each flow test, all

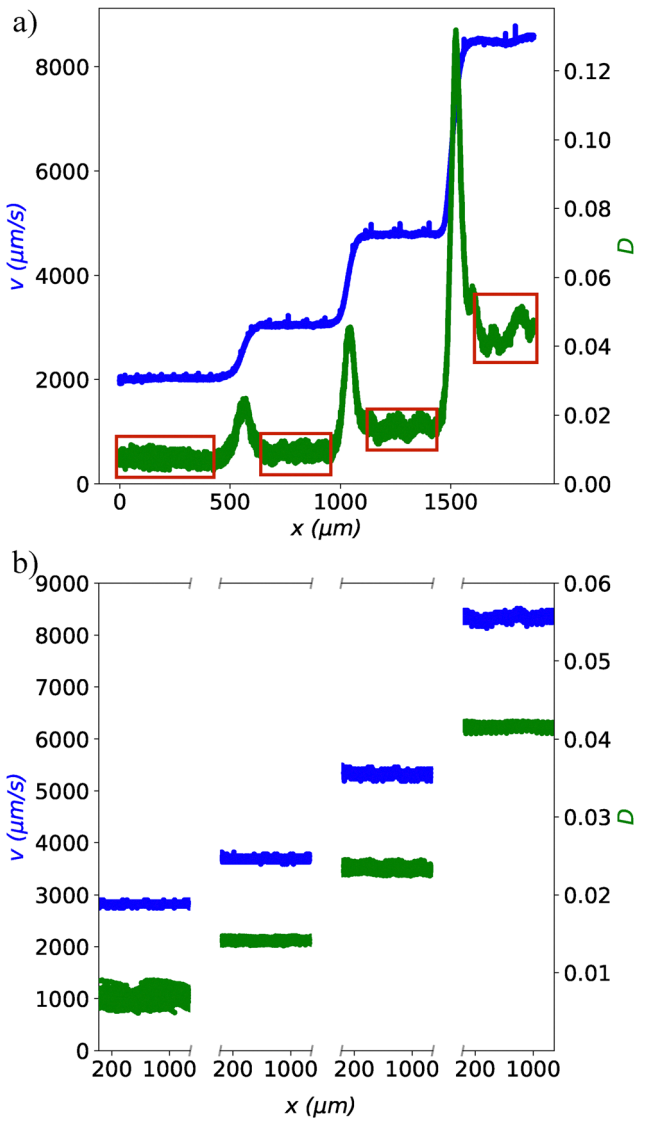

Fig. 3 Representative examples of velocity v and deformability D as a function of x in the flow direction for the linear and stacked arrangement of constrictions. For each constriction geometry, a single microscopy image captures all four constrictions of each device. In the linear arrangement, the widest constriction starts at $x \lesssim 550$ μm and the narrowest constriction ends at $x \gtrsim 1700$ μm. The red boxes indicate the region of measurement within each constriction. In the stacked arrangement, all constrictions extend the entire width of a microscopy image. Break points along the x axis indicate separate sections. For (a), data is obtained for droplets with $\chi = 1.39 \times 10^{-2}$. For (b), data is obtained for $\chi = 1 \times 10^{-3}$.

four constrictions are imaged simultaneously. Given that each individual droplet is imaged multiple times through the course of a flow test, Fig. 3a represents ~17 000 droplet measurements and Fig. 3b represents more than 36 000. In both Fig. 3a and b, as droplets travel from one constriction to the next, both v and D exhibit four individual plateaus of increasingly larger, steady values.

In Fig. 3a, the four constrictions are in-line, with the largest constriction beginning at $x = 0$ μm and the narrowest constriction ending at $x \sim 2000$ μm. Measurements of v and D are shown throughout the device, including as the droplets flow through the transitions between constrictions. In these transitions, v increases smoothly from one constriction to the next, from ~2000 μm s^{-1} in the widest constriction, to more than ~8000 μm s^{-1} in the narrowest. However, D exhibits a peak as the particles travel from one constriction to the next, indicating droplet acceleration. The front portion of the droplet moves faster than the rear, leading to an effectively higher droplet deformability as the droplet accelerates.[35] Between the third and fourth constrictions, for instance, while the plateau values of D increase from ~0.016 to ~0.045, the peak reaches nearly $D \sim 0.13$. To prevent this transition from artificially skewing measurements of D to higher values, we use the steady plateau value of D in each constriction to measure σ. These plateau regions are indicated by the red boxes in Fig. 3a.

The fast relaxation time scale associated with surface tension helps ensure the robustness of measuring deformation in steady flow. Given particles with $r_0 \sim O(10)$ μm and $\sigma \sim O(1)$ mN m^{-1}, the time scale associated with eqn (5) $\tau \sim O(10^{-4})$ s. That is, momentary perturbations in v are nearly immediately reflected in the values of D. This phenomenon can be seen clearly in the second and third constrictions in Fig. 3a. The steady values of D exhibit some degree of perturbation, which is explained by comparable perturbations in v, which may in turn be due to imperfections in the device geometry. Devices are "single-use" in that we use a new device for each flow test. Data shown in Fig. 3a corresponds to run 12 in Table S1. An additional example of data collected from a separate device using the linear arrangement of constrictions is shown in Fig. S5.

Fig. 3b shows an example of raw data collected from constrictions in the stacked configuration. Each individual constriction spans well beyond the width of the microscope image, which is ~1300 μm at 10×, as shown in Fig. 1c. As such, the transitions between the constrictions do not affect the measurements of D or v. In Fig. 3b, breakpoints in the x-axis are used to separate the measurements made within each constriction. D is plotted using a moving average over a window of 65 data points. Similar to Fig. 3a, the droplet velocity increases from $v \sim 2800$ μm s^{-1} in the widest constriction to $v \sim 8250$ μm s^{-1} in the narrowest. D increases simultaneously, from ~0.007 to ~0.042.

To ensure the applicability of steady small deformation theories, we use steady values of D to calculate surface tension, in which D is constant in both time and position along the channel, as in the regions indicated in Fig. 3a and b. By limiting our measurements to steady values of D, we avoid any flow regimes in which dilatational area change of a droplet interface can lead to rearrangement of surfactant on the surface, thus affecting surface tension.[46,62] Where D is steady, droplet position along the center line of the flow is also steady, indicating absence of cross stream migration.[52,53] Further, while the examples shown in Fig. 3a and b show measurements of D up to ~0.04, all measurements of D discussed here are below ~0.07. This magnitude of D falls well within the definition of small deformation required by the linear theories.

We use the measured values of D and v in steady flow to measure surface tension σ. Simultaneous measurements of D at different velocities confirm the linearity of D with $\dot{\gamma}$. Fig. 4a and b plot D as a function of $\mu\dot{\gamma}r_0$, with the data corresponding to the measurements shown in Fig. 3a and b. The red line in Fig. 4a is fit to a line with slope $1/\sigma$, where $\sigma = 5.78 \pm 0.53$ mN m^{-1}. The error bars on σ are propagated from the uncertainty of the linear fit. In Fig. 4, error bars on the $\mu\dot{\gamma}r_0$ axis are propagated from the standard deviation of v within each constriction, but are smaller than the size of the data points. The goodness of fit is represented by $R^2 = 0.97$. In Fig. 4b, the reciprocal slope results in a $\sigma = 6.28 \pm 0.03$ mN m^{-1} with $R^2 = 1.00$. The better fit seen in Fig. 4b demonstrates two benefits of the stacked arrangement of constrictions: more droplets are visualized in all constrictions, which span the width of the image. Further, the stacked constrictions can be imaged simultaneously at higher magnification. As a result, improved statistics are obtained even in the smaller constrictions. The measurements in Fig. 4 are obtained using the moments of inertia of the x and y axes of each droplet to calculate D (eqn (1)). We provide a detailed comparison between this and the bounding box method in Fig. S6. In short: we find the bounding box method may introduce noise on the droplet-scale, especially when deformations are very small.

D. Comparison to other techniques

To validate the microfluidic measurements, we perform pendant droplet measurements of surface tension over a range of surfactant concentrations. Fig. 5 shows the comparison between measurements made using the pendant droplet technique and steady droplet deformation in the microfluidic device, using both the linear and stacked arrangement of constrictions. We plot σ with respect to Span 80 mole fraction χ. Pendant droplet measurements are shown in blue: each data point is an average of at least seven independent droplet measurements for each χ value, with error bars indicating the standard deviation. The orange data set represents fluidic measurements obtained using the linear arrangement of constrictions, at χ values coinciding with those investigated by pendant drop. The magenta data is obtained using the stacked arrangement of constrictions at two intermediate values of χ. Each microfluidic measurement represents the results of a single flow test, with error bars representing the uncertainty in the linear fit of $D(\dot{\gamma}\mu r_0)$ for each value of χ. The SI contains details for Fig. 5: Table S1 shows the total number of droplets and total number of droplet measurements obtained at each value of χ for each flow test, for both the linear and stacked constrictions. Exact values for

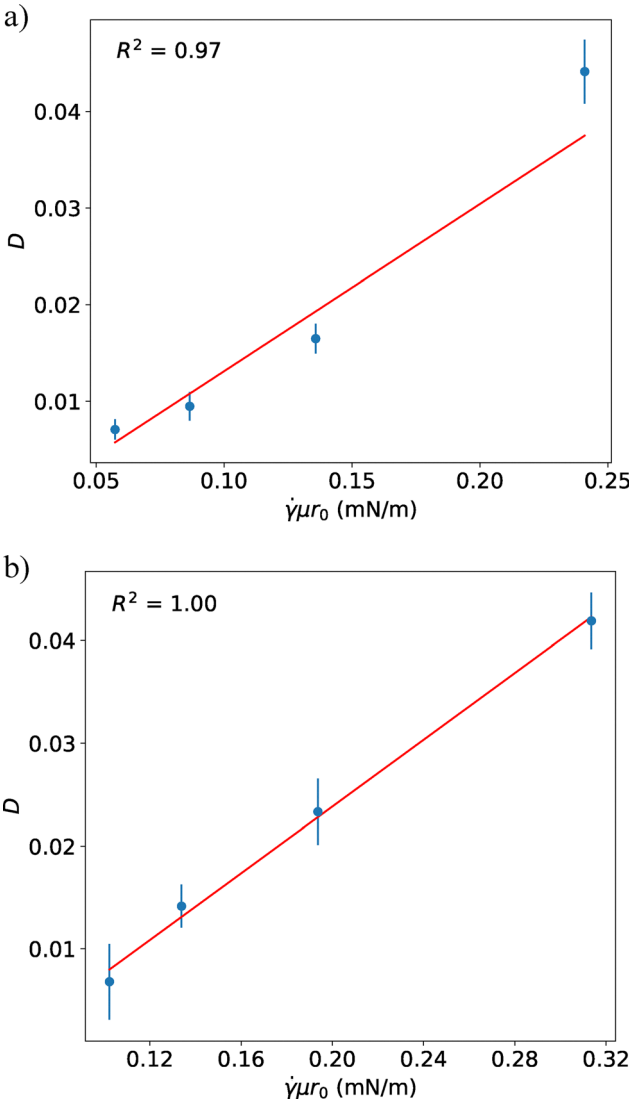

Fig. 4 Deformation, D, plotted as a function of $\dot{\gamma}\mu r_0$ for flow tests in which (a) $\chi = 1.39 \times 10^{-2}$ and (b) $\chi = 1 \times 10^{-3}$. In each plot the red line is a linear fit to the data, with slope $1/\sigma$. In (a), $\sigma = 5.78 \pm 0.53$ mN m^{-1}, and in (b), $\sigma = 6.28 \pm 0.03$ mN m^{-1}. The error bars on the data points in each plot indicate the standard deviation of the plateaus in Fig. 3a and b, respectively.

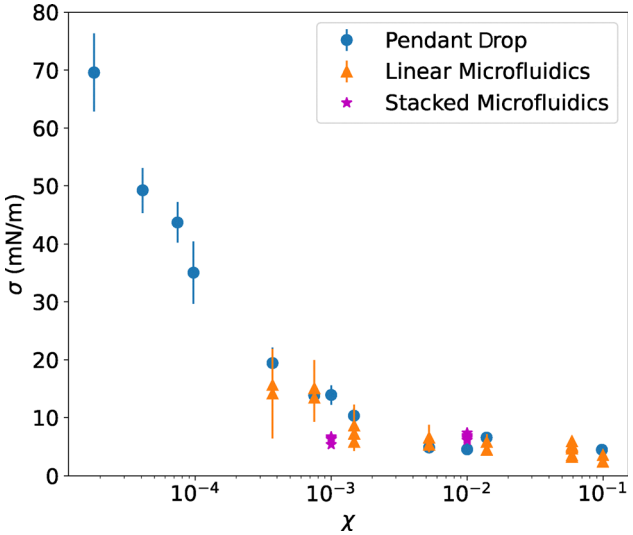

Fig. 5 Surface tension, σ, as a function of χ, the mole fractions of surfactant Span 80. Blue circles represent pendant drop measurements, with error bars representing the standard deviation based on a collection of droplets. The orange triangles and magenta stars represent fluidic measurements obtained using linear and stacked arrangements of constrictions, respectively. Each microfluidic data point represents one flow test, with error bars on σ representing the uncertainty of the linear fit in Fig. 4. Each flow test measures hundreds or thousands of droplets, as described in Table S1.

the pendant droplet and the number of trials for each data point is shown in Table S2.

In Fig. 5, surface tension decreases with surfactant concentration, with σ falling from $\sim$70 mN m^{-1} with very little surfactant down to $\sim$2 mN m^{-1} when $\chi = 0.1$. The fluidic methods measure σ from $>$15 to $<$2 mN m^{-1}. Using pendant droplet, measurements are obtained at surfactant concentration as low as $\chi = 1.8 \times 10^{-5}$, while for the microfluidic device, measurements are obtained down to $\chi = 3.7 \times 10^{-4}$. At lower values of χ than those shown for each method, droplets tend to stick to the side walls of the cuvette or microfluidic device, despite hydrophobic surface chemical pretreatments of the channels (Fig. S1). The size of the error bars decreases as χ increases for all three measurement methods: the maximum spread in the data is $\sim$15%, at $\chi = 9.7 \times 10^{-5}$, decreasing to $\sim$6% at $\chi = 9.8 \times 10^{-2}$. The size of the error bars on the fluidics measurements obtained at $\chi = 3.7$ and 7.5×10^{-4} might also be explained by the example in Fig. 4a. Measurements in the narrowest constriction of the linear arrangement may lead to an overestimation of D and thus an underestimation of σ, especially for stiffer, higher surface tension droplets. For measurements obtained using the stacked microfluidic constrictions, error bars are smaller than the size of the data points.

Fig. 5 demonstrates reasonable agreement between the microfluidic measurements of σ obtained in steady flow and the measurements obtained by pendant drop. At high surfactant concentration, beyond $\chi \sim 5 \times 10^{-3}$, surface tension drops to a nearly constant plateau, $\sigma \sim 5$ mN m^{-1}. The range of χ investigated extends both below and above the critical micelle concentration (CMC). The formation of micelles at concentrations above χ_{CMC} prevents additional free surfactant molecules from adsorbing to the water–oil interface. Measurements of χ_{CMC} may vary depending on the method used. For Span 80 in mineral oil, $\chi_{CMC} \sim 1 \times 10^{-2}$, as measured by the pendant drop and sessile drop techniques.[63] When measured by pendant drop, we observe that σ reaches a plateau at $\chi \sim 5 \times 10^{-3}$. Interestingly, when measured by fluidics, σ reaches a plateau at a slightly lower surfactant concentration, $\chi \sim 1 \times 10^{-3}$.

The lower value of χ_{CMC} observed in the fluidics measurements may be explained by appealing to the convective nature of fluidic droplet formation. Transport of surfactant to the droplet interface can be described in full detail by appealing to a mixed model that also includes Langmuir adsorption kinetics and diffusive transport. If surfactant is introduced from within the droplet phase, internal circulation within the

droplet becomes important.[64] However, in our experiments, surfactant is introduced from the external continuous phase. Further, the Peclet number is high in our flow tests, indicating that convection dominates over the diffusion of dissolved Span 80. That is, $\mathrm{Pe} = vh/D_s \sim O(10^4)$ or higher. We estimate the diffusion constant for Span 80 in mineral oil to be $D_s \sim O(10^{-8})$ cm^2 s^{-1}. Detailed studies of dynamic interfacial tension using the transient method of microfluidic tensiometry suggest that surfactant transport to the droplet interface is controlled by convection rather than diffusion.[36,65] That is, the high flow rate may facilitate adsorption of the surfactant on the droplet surface at somewhat lower concentrations than expected from pendant drop or other measurements of stationary drops.

Next, we measure surface tension using the transient fluidic technique, in which droplets exit a constriction, as in Fig. 1(d). The relaxation of the deformed droplet in the extensional flow beyond the constriction exit is used to measure σ.[34–36,54] Upon exiting the constriction, a deformed drop quickly relaxes back to its spherical shape. Fast relaxation relies on a sudden, dramatic change in droplet velocity due to a sudden change in channel width.[35,36] For this reason, we investigate droplet relaxation for expansions that are at least a factor of 5 times wider than the constriction. Eqn (7) provides the measurement of σ, which is the slope of the linear fit of the left hand side as a function of D/r_0. The details of this analysis are shown in Fig. S3 and S4. In each of our transient flow tests, σ is measured at the exit of multiple constrictions, and we report the average and standard deviation of the measurements.

In Fig. 6, we compare the steady and transient fluidic methods at two surfactant concentrations, $\chi = 10^{-2}$, in Fig. 6a, and 10^{-3}, in Fig. 6b. In this comparison, surface tension is measured as a function of λ, adjusted by adding polymer to the water droplets. We choose the uncrosslinked hydrogel polyethylene glycol diacrylate (PEGDA). With the multitude of applications for PEGDA and other polymeric solutions, understanding surface tension of PEGDA-filled drops in microchannel flows will help prevent ink clogging, facilitate coating spreadability, and improve formulation stability. PEGDA increases the viscosity of the inner phase: λ increases from 0.02 to 20 as PEGDA concentration c increases from 0 to 39%. For steady flow measurements of σ, the prefactor of eqn (2) similarly increases from $f = 1.005$ to 1.03. In the transient measurements, α in eqn (6) increases from 1.23 to 1.40. The results in Fig. 6a and b suggest that σ does not strongly vary with λ, regardless of the fluidic method used. Due to its hydrophilic nature, PEGDA may not strongly adsorb to the oil–water interface, especially given the preferential adsorption of Span 80, an amphiphile. Further, the spread in the data obtained from each fluidic method is comparable.

In Fig. 6, the data in green represents measurements obtained on stationary drops using the pendant droplet technique. Given the lack of dependence of σ on λ, pendant drop measurements are obtained without PEGDA in the water droplets, corresponding to $\lambda = 0.02$. The dotted lines represent the average, with the green shadow representing the standard deviation, of measurements on 10 or 11 unique droplets. When

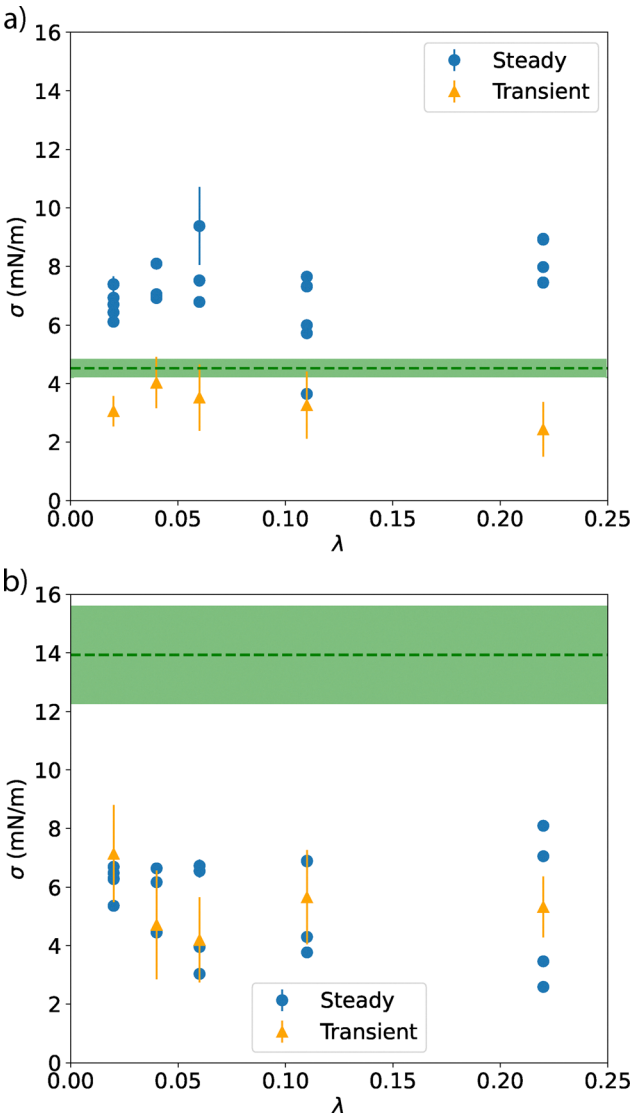

Fig. 6 Surface tension as a function of λ, controlled by adding PEGDA to water drops, with Span 80 (a) $\chi = 1 \times 10^{-2}$ and (b) $\chi = 1 \times 10^{-3}$. Steady fluidics measurements use the stacked geometry: data points represent individual flow tests with error bars propagated from the linear fit in Fig. 4. Error bars for the transient method are the standard deviation of measurements from multiple constrictions in a single flow test. The green dotted line and shadow represent the average and standard deviation of pendant drop measurements at $\lambda = 0.02$ ($c = 0\%$ PEGDA).

$\chi = 10^{-2}$, beyond the χ_{CMC} indicated in Fig. 5, measurements of σ from the pendant drop fall in between the two fluidic methods (Fig. 6a). When χ decreases to 10^{-3} in Fig. 6b, however, the pendant drop measures σ significantly higher surface tension than either fluidic method. Measurements of σ average to 5.4 ± 0.8 for the fluidic methods, regardless of whether the steady or transient method is used. The pendant drop measures $\sigma = 13.9 \pm 1.4$, nearly twice as large as the value obtained from fluidics. In all, Fig. 6 corroborates the suggestion from Fig. 5 that stationary pendant drop measurements suggests a higher value of χ_{CMC} than obtained from measurements of droplets in flow.

The steady flow shown in both Fig. 5 and 6 show one data point for each flow test, and indicate the run-to-run variation. Within each flow test, droplet size remains fairly constant. However, droplet size can vary from one flow test to the next. The constrictions in the stacked geometry are wide enough such that the droplet diameters are no more than ~70% of the constriction width. However, in many cases the channel height h is the limiting dimension of the channel. So, even when droplets do not appear confined by side walls in the two-dimensional microscopy images, they might be slightly confined in the z direction.

To check if the degree of droplet confinement in the z dimension of the channel alters deformation and measurements of surface tension, we measure σ as a function of droplet diameter a normalized by channel height h. Fig. 7 shows the steady deformation fluidic data from Fig. 6 as a function of a/h, with c given in the legend. While a/h varies from nearly 0.8 to 1.3 for the collection of all the steady deformation measurements, σ does not strongly depend on the degree of confinement: $\langle\sigma\rangle = 7.3 \pm 1.1$, a variation of 15%. We find the same to be true for the steady deformation data collected at $\chi = 10^{-3}$, in Fig. S7a. Despite a/h ranging from 0.5 and 1.3, σ shows no strong dependence on the degree of droplet confinement: $\langle\sigma\rangle = 5.5 \pm 1.5$, for a variation of 27%. A similar analysis for measurements obtained in the linear arrangement of constrictions is shown in Fig. S7b, in which a/h varies from 0.9 to 1.3 for seven different flow tests. Previous studies suggest that the optimal spacing of droplets between channel walls is $0.2 < a/h < 0.8$ while using the transient method and when λ is small. As $a/h \to 1$, lubrication forces may impact droplet velocity.[34] However, Fig. 7 shows that measurements of σ at $a/h > 1$ are comparable to those obtained when a/h is as low as ~0.5. The fact that σ does not strongly vary with a/h suggests that slight compression in the z dimension does not significantly influence the resulting measurements of σ in our measurement range of $D < 0.07$. For clean drops in confined shear flow above $D = 0.1$, confinement increases deformation, with a more pronounced increase for larger D.[48] For fully surfactant laden drops and rigid particles, the degree of confinement is a third order correction to the prefactor f in eqn (2).[50] Because our approach uses $f = 1$, confinement might explain the slightly lower value of σ obtained at $a/h \sim 1.3$ in Fig. 7.

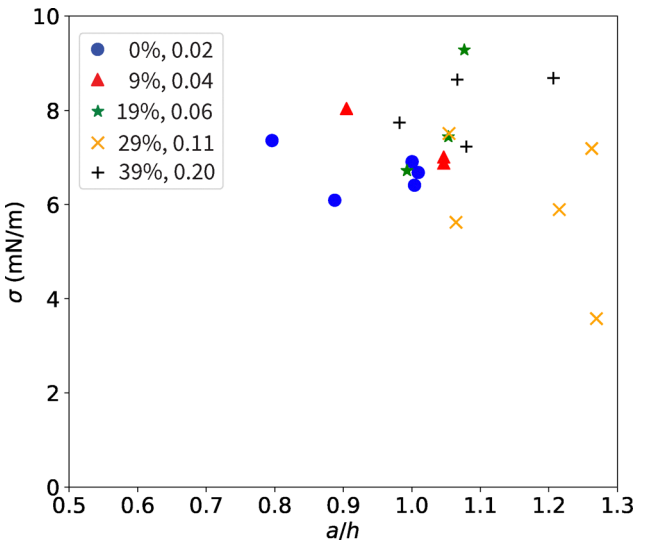

Fig. 7 Surface tension, σ, as a function of confinement, droplet diameter a divided by channel height, h. Measurements are obtained from steady deformation in stacked constrictions, with Span 80 $\chi = 10^{-2}$ and various amounts of PEGDA. The legend gives c, in volume %, and λ.

E. Alternative emulsion systems

The above discussion focuses on water droplets in oil, with non-ionic surfactant Span 80 in the oil phase, over a range of viscosity ratios $0.02 < \lambda < 0.20$. We also validate our technique on systems of oil droplets in water by using an ionic surfactant, SDS. By switching the dispersed and continuous phases, we switch from viscosity ratios from $\lambda < 1$ to $\lambda = 44$, further exploring the capabilities of this method. Broad viscosity ratios are found in biological applications using fluorinated oils as the continuous phase. Fluorinated oils are particularly useful to allow oxygen transfer to cells encapsulated in droplets and their viscosity ranges from 0.64 cP to 28.4 cP.[66–68] Water droplets in these oils have up to $\lambda \sim 32$.

Fig. 8 compares surface tension measurements obtained using pendant drop and steady measurements of deformation in a stacked microfluidic device. SDS concentration is varied between $\chi = 10^{-4}$ and 0.01. Between $\chi = 1.25 \times 10^{-3}$ and 0.005, the measurements of σ are within 16.3% of each other, with some overlapping error bars. Error bars on the pendant drop measurements represent the standard deviation of measurements obtained from at least 7 unique drops. As in Fig. 5 and 6, error bars on the fluidic measurements represent the standard error of the fit used to obtain σ.

Measuring the surface tension of mineral oil drops suspended in water, when $\lambda \gg 1$, presents several challenges. These challenges manifest especially in systems with higher surfactant concentrations, as seen for the measurement at $\chi = 0.01$ in Fig. 8. Lowering the viscosity of the continuous phase compared to the droplet phase causes an increase in droplet size. Size can be decreased by increasing the flow rate ratio of the continuous and dispersed phases.[69,70] However, increasing flow rate of the continuous phase too much may cause backflow of the dispersed phase, preventing droplet formation entirely. Given this tradeoff, we can most easily generate oil droplets with diameters down to 70 μm. Also, the continuous phase viscosity provides the viscous shear stresses, $\mu\dot{\gamma}$, required to both pinch off droplets and deform them in steady flow. Since the viscosity of water is ~40× less than that of mineral oil, the continuous fluid velocity must be increased to compensate. For instance, data shown in Fig. 8 represent droplet velocities as fast as ~0.5 m s^{-1}, which required frame rates up to 30 000 fps. Further, the higher driving pressures needed to obtain faster flow can cause device failure; our devices can withstand up to several bar.

We also measure the effect of adding non-ionic surfactant Tween 80 to the continuous phase. Table 1 shows measurements

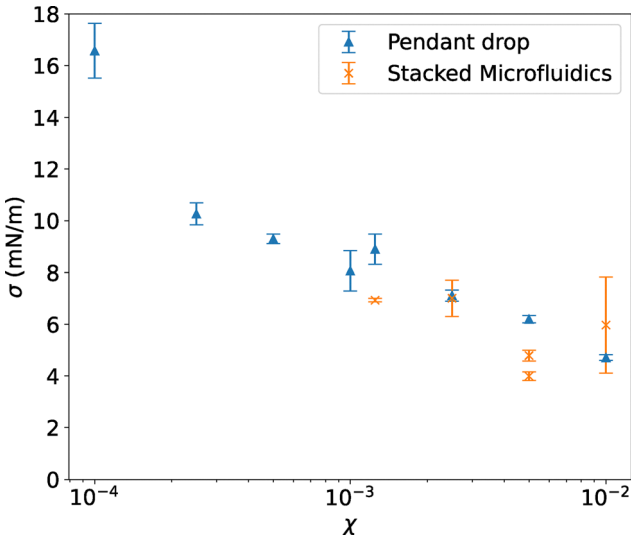

Fig. 8 Surface tension σ of oil drops in water as a function of SDS mole fraction χ using the pendant drop method (blue) and stacked steady fluidics device (orange). The error bars on the pendant drop data represent the standard deviation of at least 7 measurements for each value of χ; error bars on the fluidics data represent standard errors in the linear fit, as described in Fig. 4.

of σ for three concentrations of Tween 80: two of these represent water droplets in oil; one represents oil droplets in water. In each case Tween 80 is added to the continuous phase. However, Tween 80 is more miscible in water than in mineral oil. This miscibility can cause difficulty with water droplet pinchoff, such as tails forming at the end of droplets or oil droplets forming when water droplets are desired. The surface tension of these malformed droplets cannot be measured from droplet deformation. Also, generating and deforming oil drops in water with Tween 80 causes similar challenges to those observed with SDS. Regardless, steady deformation measures surface tension values comparable to pendant drop, for σ between $\sim$8 and 18 mN m^{-1}.

IV. Practical considerations

We suggest that steady droplet deformation measurements in the small deformation regime provide a robust way to assess surface tension with minimal geometric design requirements. We anticipate this method may benefit fluidic droplet generation for a wide variety of broader applications. Here we discuss practical considerations for implementing this method.

Our in-line tensiometry method, placed downstream of a microfluidic droplet maker, uses measurements of deformation in steady flow. Steady deformation measurements arguably represent a simpler approach than measurements of transient deformation in extensional flow. That is, steady deformation can be measured for droplets flowing through even a single constriction, as long as the unperturbed droplet size is known. Then, measurement of the steady value of D and v can suffice to measure Ca and therefore, surface tension σ. In contrast, in transient extension measurements, σ is obtained from a fit to a curve, represented by eqn (7) and shown in Fig. S4. This curve contains as many data points as there are instances of droplet shapes observed in the extensional flow, enabling a high degree of freedom in the linear fit. In steady measurements, the shape of all droplets in flow is averaged at any given shear rate to obtain σ, giving one degree of freedom for a given constriction. Multiple constrictions can be used to obtain D as a function of $\dot{\gamma}$, providing an additional degree of freedom for each constriction. Despite the fewer degrees of freedom in measuring σ in steady deformation, steady measurements of σ compare well with those obtained from both transient extension flows and pendant drop measurements.

Because measurements of σ in steady flow come from averaged values of D, care must be taken to ensure D is measured precisely. In practice, this requires sufficiently high spatial resolution and sufficiently fast time resolution. The spatial resolution, or number of pixels across each drop diameter, determines the minimum resolvable value of deformation D. When combined with the slowest droplet velocity, seen in the largest constriction, the minimum steady D therefore determines an upper limit on the measurable surface tension. Due to the importance of spatial resolution, the moment of inertia shape analysis method provides a better measure of both droplet shape and thus D as compared to the bounding box method (Fig. S6). Spatial resolution can be increased through a combination of larger drops and a higher magnification objective. However, higher magnification objectives typically reduce the transit time of a droplet through the field of view, requiring faster camera frame rates. The importance of temporal resolution likewise manifests in two ways. Images of fast-moving droplets must be captured at a rate fast enough that individual droplet shapes are well defined and not blurred. Further, frame rates must be sufficiently fast to capture single droplets multiple times in the field of view to enable particle tracking measurements of v. Temporal resolution becomes especially important when droplet viscosity is larger than the continuous phase. As discussed above, continuous phases of lower viscosity require faster linear velocities and thus even higher frame rates to capture crisp images of droplets.

Keeping these practical considerations in mind, measurements of steady deformation D even smaller than 0.01 are possible when using objective magnifications as low as 5×. When combined with measurements of $v \sim O(1000)$ μm s^{-1}, this enables measurements of σ between $\sim O(1)$ and $O(10)$ mN m^{-1}, and we measure σ up to $\sim$20 mN m^{-1}. Interestingly, resolution of the technique is not what limits measurements of larger σ. Rather, reducing c destabilizes the droplets in flow (Fig. S1).

Table 1 Measurements of surface tension obtained using pendant drop, σ_{PD} and steady fluidic deformation, σ_{SF}. The continuous phase contains Tween 80 at χ_{Tween}, forming water drops in oil (W/O) or oil drops in water (O/W)

χ_{Tween}	Droplet type	σ_{PD} (mN m^{-1})	σ_{SF} (mN m^{-1})
2×10^{-4}	W/O	17.73 ± 4.32	16.56 ± 2.13
1×10^{-3}	W/O	8.04 ± 0.57	6.63 ± 3.08
2×10^{-3}	O/W	12.05 ± 1.21	12.25 ± 0.23

The dimensional scaling argument present in small deformation theories agree well with experiments and boundary integral simulations up to approximately $D \approx 0.2$. Larger values of σ would generate smaller values of both D and Ca, thus maintaining the relevance of the small deformation scaling theories. We anticipate this approach can be extended to rigid particles, which deform similarly to fully surfactant laden drops.[47] This would enable estimates of elastic moduli from steady deformation. On the other hand, generating droplets of much larger sizes, approaching a millimeter in diameter, or those with ultra-low surface tension, would facilitate measurements to test the upper limits of D and Ca for which the linear scaling still holds. For larger droplets, the system size should be scaled up accordingly, because confinement increases deformation as Ca increases.[48]

In our validation, we compare two geometric implementations of steady flow deformation measurements. Both geometries have relatively small footprints within an overall device design, and thus may facilitate additional in-line assays to be implemented either upstream or downstream. Each device design has its advantages: the ''linear'' device may be preferred if very deformable droplets navigating curves in the channel might break up; the longer channels of the ''stacked'' device allow for better statistics in measuring D and v, especially at higher flow rates.

V. Conclusion

We demonstrate high-throughput measurements of droplet surface tension in flow using a microfluidic design that allows for in-line measurements with minimal geometric and analytical complexity. This accessibility is accomplished by measuring droplet deformation in steady flow, with sufficiently high shear rates to cause droplet deformation. Fluidic-generated droplets flow through increasingly narrow channel widths and therefore experience several distinct values of shear stress at a single driving pressure or flow rate. Video analysis provides simultaneous measurements of droplet velocity and deformability, from which we calculate surface tension. We validate our microfluidic tensiometer with both pendant drop measurements and a fluidic method that measures transient deformation in extensional flow, as droplets exit a constriction.

Importantly, our results highlight the robustness of the linear scaling arguments found throughout small droplet deformation theories. We find that steady deformation, even using a prefactor $f = 1$, provides a robust measure of surface tension in pressure-driven flows through microfluidic channels with rectangular cross-sections, even when droplet size approaches that of the narrowest channel dimension. Measurements of surface tension using steady deformation remain robust across a variety of emulsion systems. This demonstration suggests that constriction tensiometers can be reasonably incorporated into devices with rectangular cross-sections, without requiring cylindrical geometry or other design features to generate extensional flow.

Our methods can measure surface tension within a small region of interest within the architecture of a given chip and with minimal analysis or computation required. This simplicity can enable wider incorporation of tensiometry into fluidic devices that are designed for other purposes, like performing assays for biomedical research or creating formulations for cosmetics, pharmaceuticals, fertilizers or other products. Especially in formulation science, microfluidic automation is improving the accessibility of microfluidics to a wider user base.[71,72] Our device offers high potential to be incorporated within automated platforms with its ease of analysis and robust design.

Author contributions

ES and SM contributed equally to this work. ES and SMH conceptualized overarching research goals and aims. ES, SM, and AJP executed experiments, wrote and applied analysis codes, and validated research aims. SMH supervised and managed project as well as acquired project funding and resources. All authors contributed to writing, discussed the results, and approved the final manuscript.

Conflicts of interest

The authors have no conflicts of interest at this time. Some details of this work have been filed as PCT/US23/30252 on August 15, 2023, and published on February 22, 2024; publication number WO 2024/039662.

Data availability

Data are available from the corresponding author upon reasonable request.

Supplementary information: Nomenclature, additional microscopy image examples corresponding to Fig. 1, details of the transient measurement analysis, tabulated data from both the flow tests and pendant drop, additional data examples corresponding to Fig. 3, 4 and 7, comparison of the different image analysis algorithms used to measure deformation, and surface tension measurements as a function of droplet size. See DOI: **https://doi.org/10.1039/d5sm00493d**

Acknowledgements

This work was funded by the Center for Research Innovation Spark Fund at Northeastern University. The authors wish to thank Ryan Poling-Skutvik for use of the Krüss DSA-100. The authors acknowledge Charles Wallace for developing early versions of the particle tracking code used in transient measurements, Ian Steele for pendant drop measurements of surface tension with Tween 80, and Barrett Smith for helpful discussions surrounding device designs.

References

1 D. J. Mcclements, Critical review of techniques and methodologies for characterization of emulsion stability, *Crit. Rev. Food Sci. Nutr.*, 2007, **47**, 611–649.

2 M. Kakran and M. N. Antipina, Emulsion-based techniques for encapsulation in biomedicine, food and personal care, *Curr. Opin. Pharmacol.*, 2014, **18**, 47–55. Anti-infectives • New technologies.

3 E. Amstad, M. Chemama, M. Eggersdorfer, L. R. Arriaga, M. P. Brenner and D. A. Weitz, Robust scalable high throughput production of monodisperse drops, *Lab Chip*, 2016, **16**, 4163–4172.

4 J. Wu, S. Yadavali, D. Lee and D. A. Issadore, Scaling up the throughput of microfluidic droplet-based materials synthesis: A review of recent progress and outlook, *Appl. Phys. Rev.*, 2021, **8**, 031304.

5 S. Yadavali, D. Lee and D. Issadore, Robust microfabrication of highly parallelized three-dimensional microfluidics on silicon, *Sci. Rep.*, 2019, **9**, 12213.

6 J. Nunes, S. Tsai, J. Wan and H. A. Stone, Dripping and jetting in microfluidic multiphase flows applied to particle and fibre synthesis, *J. Phys. D: Appl. Phys.*, 2013, **46**, 114002.

7 L. Chen, Y. Xiao, Q. Wu, X. Yan, P. Zhao, J. Ruan, J. Shan, D. Chen, D. A. Weitz and F. Ye, Emulsion designer using microfluidic three-dimensional droplet printing in droplet, *Small*, 2021, **17**, 2102579.

8 J.-W. Kim, S. H. Han, Y. H. Choi, W. M. Hamonangan, Y. Oh and S.-H. Kim, Recent advances in the microfluidic production of functional microcapsules by multiple-emulsion templating, *Lab Chip*, 2022, **22**, 2259–2291.

9 W. Wang, B.-Y. Li, M.-J. Zhang, Y.-Y. Su, D.-W. Pan, Z. Liu, X.-J. Ju, R. Xie, Y. Faraj and L.-Y. Chu, Microfluidic emulsification techniques for controllable emulsion production and functional microparticle synthesis, *Chem. Eng. J.*, 2023, **452**, 139277.

10 S. Fouilloux, F. Malloggi, J. Daillant and A. Thill, Aging mechanism in model pickering emulsion, *Soft Matter*, 2016, **12**, 900–904.

11 W. Sun, X. Zhang, C. Yao, Q. Wang, N. Jin, H. Lv and Y. Zhao, Hydrodynamic characterization of continuous flow of pickering droplets with solid nanoparticles in microchannel reactors, *Chem. Eng. Sci.*, 2021, **245**, 116838.

12 Q. Zhou, Y. Sun, S. Yi, K. Wang and G. Luo, Investigation of droplet coalescence in nanoparticle suspensions by a microfluidic collision experiment, *Soft Matter*, 2016, **12**, 1674–1682.

13 N. Amiri, J. M. Prisaznuk, P. Huang, P. R. Chiarot and X. Yong, Deep-learning-enhanced modeling of electrosprayed particle assembly on non-spherical droplet surfaces, *Soft Matter*, 2025, **21**, 613–625.

14 D. J. Collins, A. Neild, A. deMello, A.-Q. Liu and Y. Ai, The Poisson distribution and beyond: methods for microfluidic droplet production and single cell encapsulation, *Lab Chip*, 2015, **15**, 3439–3459.

15 T. Alkayyali, T. Cameron, B. Haltli, R. Kerr and A. Ahmadi, Microfluidic and cross-linking methods for encapsulation of living cells and bacteria-a review, *Anal. Chim. Acta*, 2019, **1053**, 1–21.

16 S. D. Ling, Y. Geng, A. Chen, Y. Du and J. Xu, Enhanced single-cell encapsulation in microfluidic devices: From droplet generation to single-cell analysis, *Biomicrofluidics*, 2020, **14**, 061508.

17 E. Santini, L. Liggieri, L. Sacca, D. Clausse and F. Ravera, Interfacial rheology of span 80 adsorbed layers at paraffin oil-water interface and correlation with the corresponding emulsion properties, *Colloids Surf., A*, 2007, **309**, 270–279.

18 I. B. Ivanov and P. A. Kralchevsky, Stability of emulsions under equilibrium and dynamic conditions, *Colloids Surf., A*, 1997, **128**, 155–175.

19 S. Dukhin, J. Sjöblom, D. Wasan and Ø. Sæther, Coalescence coupled with either coagulation or flocculation in dilute emulsions, *Colloids Surf., A*, 2001, **180**, 223–234.

20 R. F. Lee, Agents which promote and stabilize water-in-oil emulsions, *Spill Sci. Technol. Bull.*, 1999, **5**, 117–126.

21 W. Guan, W. Zhou, C. Lu and B. Zhong Tang, Synthesis and design of aggregation-induced emission surfactants: Direct observation of micelle transitions and microemulsion droplets, *Angew. Chem.*, 2015, **54**, 15160–15164.

22 R. Petkova, S. Tcholakova and N. D. Denkov, Foaming and foam stability for mixed polymer–surfactant solutions: Effects of surfactant type and polymer charge, *Langmuir*, 2012, **28**, 4996–5009.

23 J. Drelich, C. Fang and C. L. White, Measurement of Interfacial Tension in Fluid-Fluid Systems, *Encyclopedia of Surface and Colloid Science*, Marcel Dekker Inc, New York City, NY, 2002, pp. 3152–3166.

24 P. Roy, S. Liu and C. S. Dutcher, Droplet interfacial tensions and phase transitions measured in microfluidic channels, *Annu. Rev. Phys. Chem.*, 2021, **72**, 73–97.

25 C. D. Manning and L. E. Scriven, On interfacial tension measurement with a spinning drop in gyrostatic equilibrium, *Rev. Sci. Instrum.*, 1977, **48**, 1699–1705.

26 S. Choi, Y. Kwon and J. Lee, Electrowetting-based measurement of interfacial tension, *Appl. Phys. Lett.*, 2014, **105**, 183509.

27 Y.-C. Liao, O. A. Basaran and E. I. Franses, Hydrodynamic effects on the oscillations of supported bubbles: implications for accurate measurements of surface properties, *Colloids Surf., A*, 2004, **250**, 367–384, in honour of the 250th volume of Colloid and Surfaces A and the 25th Anniversary of the International Association of Colloid and Interface Scientists (IACIS).

28 S. Goel, N. Joshi, M. S. Uddin, S. Ng, E. Acosta and A. Ramachandran, Interfacial tension of the water-diluted bitumen interface at high bitumen concentrations measured using a microfluidic technique, *Langmuir*, 2019, **35**, 15710–15722, DOI: **10.1021/acs.langmuir.9b02253**, pMID: 31631660.

29 L.-J. Yang, K.-C. Liu and W.-C. Lin, *et al.*, On deriving surface tension force in mems, *J. Appl. Sci. Eng.*, 2014, **17**, 223–230.

30 G. I. Taylor, The formation of emulsions in definable fields of flow, *Proc. R. Soc. London, Ser. A*, 1934, **146**, 501–523,

containing papers of a mathematical and physical character.
31 J. Rallison, The deformation of small viscous drops and bubbles in shear flows, *Annu. Rev. Fluid Mech.*, 1984, **16**, 45–66.
32 V. Preziosi and G. Tomaiuolo, Microcapillary flow method to investigate emulsion droplet deformability, *AIP Conf. Proc.*, 2020, **2257**, 020004.
33 M. M. Villone, J. K. Nunes, Y. Li, H. A. Stone and P. L. Maffettone, Design of a microfluidic device for the measurement of the elastic modulus of deformable particles, *Soft Matter*, 2019, **15**, 880–889.
34 J. T. Cabral and S. D. Hudson, Microfluidic approach for rapid multicomponent interfacial tensiometry, *Lab Chip*, 2006, **6**, 427–436.
35 S. D. Hudson, J. T. Cabral, W. J. Goodrum Jr, K. L. Beers and E. J. Amis, Microfluidic interfacial tensiometry, *Appl. Phys. Lett.*, 2005, **87**, 081905.
36 Y. Chen and C. S. Dutcher, Size dependent droplet interfacial tension and surfactant transport in liquid–liquid systems, with applications in shipboard oily bilgewater emulsions, *Soft Matter*, 2020, **16**, 2994–3004.
37 D. Baah and T. Floyd-Smith, Microfluidics for particle synthesis from photocrosslinkable materials, *Microfluid. Nanofluid.*, 2014, **17**, 431–455.
38 J. C. McDonald, D. C. Duffy, J. R. Anderson, D. T. Chiu, H. Wu, O. J. Schueller and G. M. Whitesides, Fabrication of microfluidic systems in poly (dimethylsiloxane), *Electrophoresis*, 2000, **21**, 27–40.
39 A. R. Abate, D. Lee, T. Do, C. Holtze and D. A. Weitz, Glass coating for pdms microfluidic channels by sol–gel methods, *Lab Chip*, 2008, **8**, 516–518.
40 C. Trégouët, T. Salez, C. Monteux and M. Reyssat, Transient deformation of a droplet near a microfluidic constriction: A quantitative analysis, *Phys. Rev. Fluids*, 2018, **3**, 053603.
41 J. C. Crocker and D. G. Grier, Methods of digital video microscopy for colloidal studies, *J. Colloid Interface Sci.*, 1996, **179**, 298–310.
42 J. D. Berry, M. J. Neeson, R. R. Dagastine, D. Y. Chan and R. F. Tabor, Measurement of surface and interfacial tension using pendant drop tensiometry, *J. Colloid Interface Sci.*, 2015, **454**, 226–237.
43 J. Jennings Jr and N. Pallas, An efficient method for the determination of interfacial tensions from drop profiles, *Langmuir*, 1988, **4**, 959–967.
44 E. Huang, A. Skoufis, T. Denning, J. Qi, R. R. Dagastine, R. F. Tabor and J. D. Berry, Opendrop: Open-source software for pendant drop tensiometry contact angle measurements, *J. Open Source Software*, 2021, **6**, 2604.
45 Y. Rotenberg, L. Boruvka and A. Neumann, Determination of surface tension and contact angle from the shapes of axisymmetric fluid interfaces, *J. Colloid Interface Sci.*, 1983, **93**, 169–183.
46 H. A. Stone and L. G. Leal, The effects of surfactants on drop deformation and breakup, *J. Fluid Mech.*, 1990, **220**, 161–186.
47 P. M. Vlahovska, J. Bławzdziewicz and M. Loewenberg, Small-deformation theory for a surfactant-covered drop in linear flows, *J. Fluid Mech.*, 2009, **624**, 293–337.
48 V. Sibillo, G. Pasquariello, M. Simeone, V. Cristini and S. Guido, Drop deformation in microconfined shear flow, *Phys. Rev. Lett.*, 2006, **97**(5), 054502.
49 M. Shapira and S. Haber, Low reynolds number motion of a droplet in shear flow including wall effects, *Int. J. Multiphase Flow*, 1990, **16**, 305–321.
50 M. Villone, F. Greco, M. Hulsen and P. Maffettone, Simulations of an elastic particle in newtonian and viscoelastic fluids subjected to confined shear flow, *J. Non-Newtonian Fluid Mech.*, 2014, **210**, 47–55.
51 C. Coulliette and C. Pozrikidis, Motion of an array of drops through a cylindrical tube, *J. Fluid Mech.*, 1998, **358**, 1–28.
52 H. Zhou and C. Pozrikidis, Pressure-driven flow of suspensions of liquid drops, *Phys. Fluids*, 1994, **6**, 80–94.
53 J. T. Schwalbe, F. R. Phelan Jr, P. M. Vlahovska and S. D. Hudson, Interfacial effects on droplet dynamics in poiseuille flow, *Soft Matter*, 2011, **7**, 7797–7804.
54 D. Lee and A. Q. Shen, Interfacial tension measurements in microfluidic quasi-static extensional flows, *Micromachines*, 2021, **12**, 272.
55 D. Lee, C. Fang, A. S. Ravan, G. G. Fuller and A. Q. Shen, Temperature controlled tensiometry using droplet microfluidics, *Lab Chip*, 2017, **17**, 717–726.
56 Y. Chen, S. Narayan and C. S. Dutcher, Phase-dependent surfactant transport on the microscale: Interfacial tension and droplet coalescence, *Langmuir*, 2020, **36**, 14904–14923, DOI: **10.1021/acs.langmuir.0c02476**, pMID: 33269588.
57 N. J. Alvarez, L. M. Walker and S. L. Anna, A microtensiometer to probe the effect of radius of curvature on surfactant transport to a spherical interface, *Langmuir*, 2010, **26**, 13310–13319, DOI: **10.1021/la101870m**, pMID: 20695573.
58 F. Jin, R. Balasubramaniam and K. J. Stebe, Surfactant adsorption to spherical particles: The intrinsic length scale governing the shift from diffusion to kinetic-controlled mass transfer, *J. Adhes.*, 2004, **80**, 773–796, DOI: **10.1080/00218460490480770**.
59 S. Narayan, D. B. Moravec, B. G. Hauser, A. J. Dallas and C. S. Dutcher, Removing water from diesel fuel: Understanding the impact of droplet size on dynamic interfacial tension of water-in-fuel emulsions, *Energy Fuels*, 2018, **32**, 7326–7337, DOI: **10.1021/acs.energyfuels.8b00502**.
60 J. Blawzdziewicz, E. Wajnryb and M. Loewenberg, Hydrodynamic interactions and collision efficiencies of spherical drops covered with an incompressible surfactant film, *J. Fluid Mech.*, 1999, **395**, 29–59.
61 S. Guido and V. Preziosi, Droplet deformation under confined poiseuille flow, *Adv. Colloid Interface Sci.*, 2010, **161**, 89–101, physico-chemical and flow behaviour of droplet based systems.
62 H. A. Stone, A simple derivation of the time-dependent convective-diffusion equation for surfactant transport along a deforming interface, *Phys. Fluids A*, 1990, **2**, 111–112.
63 S. Bashir, X. C. I. Solvas, M. Bashir, J. M. Rees and W. B. J. Zimmerman, Dynamic wetting in microfluidic droplet formation, *BioChip J.*, 2014, **8**, 122–128.

64 J. D. Martin and S. D. Hudson, Mass transfer and interfacial properties in two-phase microchannel flows, *New J. Phys.*, 2009, **11**, 115005.
65 Q. Brosseau, J. Vrignon and J.-C. Baret, Microfluidic dynamic interfacial tensiometry (dit), *Soft Matter*, 2014, **10**, 3066–3076.
66 J. Clausell-Tormos, D. Lieber, J.-C. Baret, A. El-Harrak, O. J. Miller, L. Frenz, J. Blouwolff, K. J. Humphry, S. Köster, H. Duan, C. Holtze, D. A. Weitz, A. D. Griffiths and C. A. Merten, Droplet-based microfluidic platforms for the encapsulation and screening of mammalian cells and multicellular organisms, *Chem. Biol.*, 2008, **15**, 427–437.
67 J.-C. Baret, Surfactants in droplet-based microfluidics, *Lab Chip*, 2012, **12**, 422–433.
68 G. Etienne, M. Kessler and E. Amstad, Influence of fluorinated surfactant composition on the stability of emulsion drops, *Macromol. Chem. Phys.*, 2017, **218**, 1600365.
69 J. Yao, F. Lin, H. S. Kim and J. Park, The effect of oil viscosity on droplet generation rate and droplet size in a t-junction microfluidic droplet generator, *Micromachines*, 2019, **10**, 808.
70 J. Wacker, V. Parashar and M. Gijs, Influence of oil type and viscosity on droplet size in a flow focusing microfluidic device, *Procedia Chem.*, 2009, **1**, 1083–1086, proceedings of the Eurosensors XXIII conference.
71 O. Land, W. D. Seider and D. Lee, Convolutional neural network augmented soft-sensor for autonomous microfluidic production of uniform bubbles, *Chem. Eng. J.*, 2024, **499**, 156494.
72 A. E. Siemenn, E. Shaulsky, M. Beveridge, T. Buonassisi, S. M. Hashmi and I. Drori, A machine learning and computer vision approach to rapidly optimize multiscale droplet generation, *ACS Appl. Mater. Interfaces*, 2022, **14**, 4668–4679.

